Chapter 6
Resistive Switching Models by Ion Migration in Metal Oxides

Daniele Ielmini

Abstract Resistive switching in metal oxides is considered one of the most promising storage concept for future generations of nanoscaled nonvolatile memories. In bipolar resistive switching, the resistance of a conductive filament (CF) is controlled through the application of electrical stimuli, and the conductive state of the nanoscaled CF can be used to encode the value of the logical bit in a nonvolatile memory. To investigate the scaling opportunities of the resistive switching concept, physical models must be developed. This chapter summarizes the current state understanding of bipolar resistive switching, providing evidence for the voltage across the device being the controlling parameter for the CF growth during set. A physical model for set and reset transition is then described, allowing for an interpretation of the observed switching characteristics for different timescales. Finally, the open challenges for the scaling and the reliability of resistive switching memories are briefly summarized.

6.1 Introduction

The resistive-switching memory (RRAM) is an emerging memory device based on the reversible change of resistance in an active material, usually a metal oxide (e.g., NiO, TiO_2, HfO_x, TaO_x) [1–5] or a chalcogenide glass (e.g., GeSe, GeS) [6, 7]. The change of resistance is generally due to the formation and the dissolution of a conductive filament (CF) with a size of a few nanometers. The CF is initially created by a dielectric breakdown process, similar to the one observed in silicon dioxide [8–10]. In metal oxides, the material degradation due to high field and high temperature during breakdown results in a local transformation of the insulating

D. Ielmini (✉)
Dipartimento di Elettronica e Informazione and IU.NET, Politecnico di Milano,
Piazza L. da Vinci 32, 20133 Milano (MI), Italy
e-mail: ielmini@elet.polimi.it

Fig. 6.1 SEM image of a conductive nanofilament, in a Pt–CuO–Pt resistive switching memories. Reprinted with permission from [2] (©2008 Elsevier Ltd.)
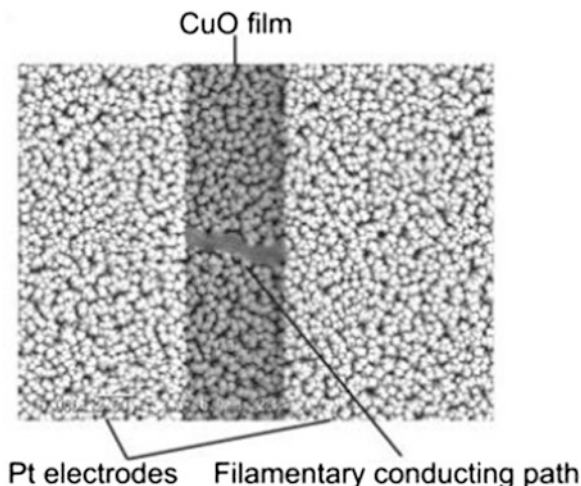
active layer into a conductive phase, e.g., a metal [11] or an oxygen-deficient region with relatively high conductivity [12, 13]. Figure 6.1 shows a scanning electron microscopy (SEM) image of a typical CF in a Pt–CuO–Pt RRAM, supporting the localized nature of the switching [2]. Other reports have indicated that the CF in TiO_2 RRAM consists of Ti_4O_7, a Magneli phase of titanium oxide exhibiting metallic conductivity [12]. For reference, oxygen-deficient silicon oxide was also found at the breakdown spot of the gate dielectric in MOS devices [9, 10]. In chalcogenide-based RRAM, instead, the CF originates from electrodeposition of cations, such as Ag and Cu, from one electrode to the other due to field- and temperature-induced electrochemical reactions [6, 7]. These electrochemical devices are generally referred to as conductive-bridge memory (CBRAM) and can also feature silicon or metal oxides as active layers or electrolytes [14, 15].

The first observations of reversible switching in metal oxides date back to the 1960s, demonstrating electrically induced resistance change in NiO [16], TiO_2 [17], and Nb_2O_5 [18]. Most recently, resistive switching was shown to take place in ternary oxides such as Cr-doped $SrTiO_3$ [19] and ferroelectric $Pb(Zr_{0.52}Ti_{0.48})O_3$ (PZT) [20]. In the last decade, intensive industrial and academic research on RRAM devices has resurfaced for several binary metal oxides, such as NiO [21–24], TiO_x [25–28], CuO_x [29], HfO_x [30, 31], and TaO_x [32, 33]. These works have aimed at evaluating the potential of the new technology in terms of scalability in view of a possible replacement of Flash memories for high-density nonvolatile storage and memories. From this standpoint, RRAM is most attractive for ultrascaled nonvolatile memories below the 10 nm node, due to its low and controllable programming current and fast switching, resulting in a low switching energy. For instance, a programming current below 10 μA was reported thanks to the control of the CF size through a transistor in series with the RRAM device, in the so-called one transistor/one resistor (1T1R) structure [34–37]. Programming currents in the range of a few μA have also been reported in other instances [38–40]. On the other hand,

programming times in the range of a few ns or even less have been reported [40–42]. As a reference, considering a programming current of 1 µA with a programming time of 1 ns with a programming voltage of 1 V, a switching energy of 1 fJ is obtained. For comparison, the switching time in SRAM and DRAM is in the range of 3–10 ns with a switching energy of around 10 pJ, which highlights the strong potential of RRAM as a possible replacement of both nonvolatile and computer (system) memories. The area scaling of RRAM also seems promising, given the small size of the CF, together with the reported capability to control the CF size through limitation of the programming current during the formation stage [36, 37].

Although promising from several different aspects, including area scaling, switching speed, and energy consumption, RRAM still faces some fundamental limits. First, industrial development of RRAM will be possible only if this technology is demonstrated to be scalable enough to cover two or three technology nodes, otherwise the return of the industrial investments would not be sufficient. Second, reliability issues are still not completely understood, particularly in terms of cycling endurance, namely the number of program/erase cycles that can be achieved in one cell, and data retention, namely the maximum lifetime of the memory state. In particular, the low cycling endurance might critically limit the applicability of RRAM for system memories replacing SRAM and DRAM. To best address such scalability and reliability issues, the physical mechanisms must be thoroughly understood and physically based models must be developed, thus allowing for accurate prediction of scalability and for improvement and optimization of reliability.

This chapter will cover the current status about the understanding of switching and reliability mechanisms in bipolar switching RRAM. First, memory operation, including formation and program/erase switching in unipolar and bipolar memory devices, will be described. Then, the microscopic mechanisms for the resistive switching will be discussed based on experimental results obtained from HfO_x RRAM devices. A physical model for resistive switching will be shown, demonstrating the ability to predict switching parameters, such as resistance in the low resistance state and programming current as a function of operating conditions, such as the maximum current during CF formation. Finally, the reduction of switching time, switching energy, and CF size and their reliability implications will be addressed.

6.2 Unipolar, Bipolar, and Complementary Switching Characteristics

Figure 6.2 shows typical *I–V* characteristics including the resistive switching transitions for (a) unipolar, (b) bipolar, and (c) complementary switching operations. In all cases, two transitions can be identified, namely a set transition for achieving a low resistance state and a reset transition to achieve a high resistance state. The low and high resistance states will be referred to as set and reset states in the following.
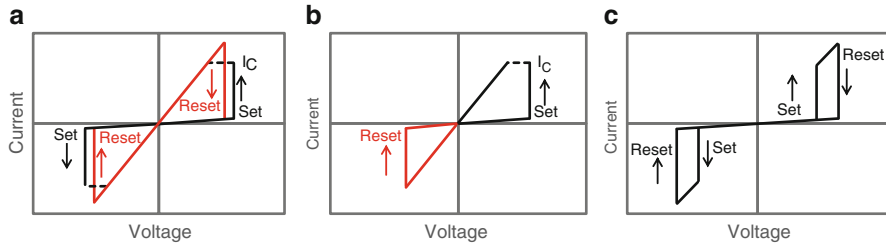
Fig. 6.2 Schematic current-voltage characteristics for the three switching modes of filamentary RRAMs, namely unipolar switching (**a**), bipolar switching (**b**), and complementary switching (**c**). Set/reset transitions occur independent of the bias polarity in unipolar switching, while they must be operated at opposite polarity in bipolar switching, e.g., set transition at positive polarity and reset transition at negative polarity. The maximum current flowing through the device after set is limited at a compliance current I_C in both unipolar and bipolar switching. In complementary switching, set with no I_C-limitation is followed by reset at the same polarity, allowing for the transition from a high resistive state to a different high resistive state. The two states differ by the position of the reservoir of conductive ions, see Fig. 6.3. Application of a negative sweep allows achieving the initial high resistive state through set and reset transitions

In unipolar switching (Fig. 6.2a), set and reset can be operated irrespective of the voltage polarity, while in bipolar switching set and reset are achieved under opposite polarities, e.g., positive voltage for set and negative voltage for reset (Fig. 6.2b). Complementary switching features instead set and reset transitions at both positive and negative polarity (Fig. 6.2c) [43]. Complementary switching was first introduced for ad hoc, antiserially connected RRAM stacks [44], then demonstrated as a fundamental switching mode in individual oxide layers in [43].

In the unipolar-switching case, the I–V curve of the reset state (OFF state in Fig. 6.2a) displays a sudden set transition at a relatively large voltage, where the device achieves a low resistance through formation (or re-activation) of the CF. In general, a current compliance I_C ("cc" in Fig. 6.2a), namely a limitation in the total current flowing through the device, is enforced during the set transition to prevent excessive growth of the CF which may eventually result in an irreversible breakdown [36, 37]. The I–V curve in the set state displays a reset transition at a reset voltage V_{reset} and a reset current I_{reset}. Reset is due to the dissolution of the CF, resulting in the transition to a high resistance state. No compliance is enforced during the reset current, thus allowing the necessary voltage and current to reach the values which are needed to dissolve the CF. The possible shape of the CF is schematically shown in Fig. 6.3 for the (a) set and (b) reset states. The conductive species are believed to diffuse radially or vertically from the CF at the hottest location during reset, as a result of thermally activated diffusion and migration [45].

In the bipolar switching case, the I–V curves in Fig. 6.2b display instead the set transition at a relatively large, positive voltage, while the reset transition takes place under a relatively low negative voltage. Note that the polarity may change depending on the particular active material/stack and on the initial forming
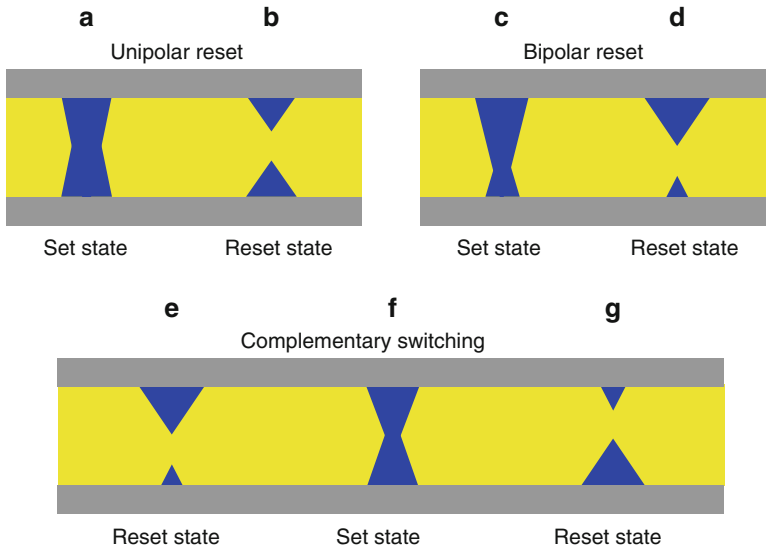
Fig. 6.3 Schematic illustration of the set and reset states in unipolar, bipolar, and complementary switching. Set state corresponds to a continuous CF in any case, while the reset state may differ depending on the polarity of the set/reset processes. In unipolar switching, set (**a**) and reset (**b**) states correspond to a continuous and interrupted CF, respectively, where filament breakdown is supposed to take place in the middle of the CF due to local temperature increase and consequent diffusion and oxidation. In bipolar switching, set (**c**) and reset (**d**) states correspond to a continuous and a interrupted filament, respectively, both with asymmetric structure due to the presence of a reservoir of conductive ions at one electrode (the top electrode in the scheme reported here). A negative applied voltage results in the transition from (**c**) to (**d**), as positively charged ions are attracted toward the top electrode by the electric field. In complementary switching, a positive applied voltage results in the transition from an initial reset state, corresponding to ions accumulated at the top electrode (**e**), to a set state, where ions are distributed along a continuous CF (**f**). A further increase of the applied positive voltage leads to the accumulation of conductive ions to the bottom electrode, thus resulting in a second reset state (**g**). Application of a voltage sweep with negative polarity results in the reverse transition, from (**g**) to (**e**) through set and reset transitions

operation. However, bipolar switching always requires voltage polarity reversal for repeatable set and reset processes. Figure 6.3c, d show the set and reset states, respectively, assuming that a positive (negative) voltage applied to the top electrode results in set (reset) transition. Most of the conductive ions are believed to remain at the top electrode, resulting in an asymmetric (e.g., conical) shape of the CF in the set state. Set and reset transitions mostly take place through vertical ion migration, activated by the temperature in the direction of the electric field.

Finally, the complementary switching characteristics in Fig. 6.2c were recently demonstrated for bipolar switching devices such as HfO$_x$ RRAM [43]. In complementary switching, the set transition under positive voltage applied to the top electrode is not limited by any compliance, therefore the CF achieves a maximum size which is only limited by the amount of available conductive ions (e.g., hafnium ions Hf$^+$ or oxygen vacancies V$_O^+$) in the switching location. After completion of

CF growth, the voltage is further increased, leading to the migration of conductive ions toward the negative (bottom) electrode and to a consequent deactivation of the CF, resulting in a reset transition at a relatively large voltage. After reset, almost all ions that contributed to the formation and growth of the CF are located at the bottom negative electrode side and the resistance is relatively high, given the absence of a continuous CF. A similar operation is then carried out under negative voltage applied to the top electrode, leading to ion migration from the reservoir located at the bottom electrode toward the top electrode. This leads to a set transition, i.e., CF nucleation and growth, followed by reset, i.e., CF dissolution due to further ion migration toward the top negative electrode [43]. The same sequence can be further repeated until a maximum number of cycles, limited by the endurance lifetime. Complementary switching was first demonstrated in ad hoc stacks, consisting of a metal–insulator–metal–insulator–metal (MIMIM) structure where the intermediate electrode served as the initial reservoir for cations (positively charge ions), e.g., Cu or Ag ions [44, 46]. The application advantage of complementary switching is that the two states encoding the logic bit have both high resistances, since they consist of the conductive ions being accumulated either toward the top or the bottom electrode. The absence of a low resistance state in the array allows purely passive crossbar arrays to be achieved without the need for any select device, e.g., diodes or threshold switches [47–57]. The two states can be recognized through the sensing of the current response to a positive voltage at the top electrode: a set/reset sequence is observed if ions are located at the top electrode, but not if they are at the bottom electrode, thus allowing the recognition of the internal logic state. Note that reading is destructive, since ions are displaced from their original location. Figure 6.3e–g shows the CF shape in the high resistance state with conductive ions at the top electrode in the set state and in the high resistance state with conductive ions at the bottom electrode, respectively. The application of a positive voltage to the high resistance state in Fig. 6.3e results in ion migration toward the bottom electrode, leading to the formation of a continuous CF (set state in Fig. 6.3f) and to the accumulation of ions at the bottom electrode (reset state in Fig. 6.3g). The reverse path is followed if a negative sweep is applied to the state in Fig. 6.3g.

A general question regarding unipolar, bipolar, and complementary switching is what mechanisms drive the set/reset transitions and what is the connection between the existence of a certain type of switching and the active material properties. In general, unipolar switching is attributed to thermochemical mechanisms, namely physical mechanisms driven by the temperature alone, with little or no role of the electric field direction [4]. Set is explained as a chemical reduction of the metal oxide, e.g., $NiO \rightarrow Ni + O$, due to the high temperature achieved at the CF site during set. Reset is instead generally explained as the inverse chemical reaction, namely oxidation, e.g., $Ni + O \rightarrow NiO$, occurring at the metal-rich CF due to the large local temperatures during voltage application [58]. Note that oxidation and reduction may generally occur in the same material system (e.g., NiO) depending on the temperature range, i.e., reduction and oxidation requires a relatively high and low temperature, respectively [4, 59, 60]. For bipolar switching, instead, the driving force for switching is believed to be the ion migration induced by the electric field

and accelerated by the local temperature due to Joule heating [45, 61]. Typical unipolar switching materials are NiO [4, 11, 21–24, 34, 36, 37, 49, 62, 63], TiO_2 [12, 27, 28], and TiON [64, 65], while bipolar switching materials include TiO_2 [25–27, 32], HfO_x [30, 31, 43], and WO_x [40]. In several cases, a coexistence between unipolar and bipolar switching has been observed, namely materials capable of bipolar switching were demonstrated to feature also unipolar switching [38, 66–69].

6.3 Bipolar Switching Characteristics

Figure 6.4 shows the measured I–V characteristics for a bipolar switching RRAM with HfO_x active oxide and TiN as electrode material in both the top and bottom contacts [70]. The thickness of the oxide layer was 20 nm, and the electrical switching was initiated by a forming stage at about +3 V (not shown). Set and reset transitions were observed under positive and negative voltage, respectively. The figure shows three I–V characteristics with a set/reset transition for increasing current compliance I_C enforced during the set transition, namely $I_C = 0.5, 0.75$, and 1 mA. The set transition occurs almost abruptly at about 0.5 V. Immediately after set, the current is limited to I_C while the voltage drop across the device reaches a value V_C of about 0.4 V. The resistance of the device in the set state is given by:

$$R = V_C/I_C, \tag{6.1}$$
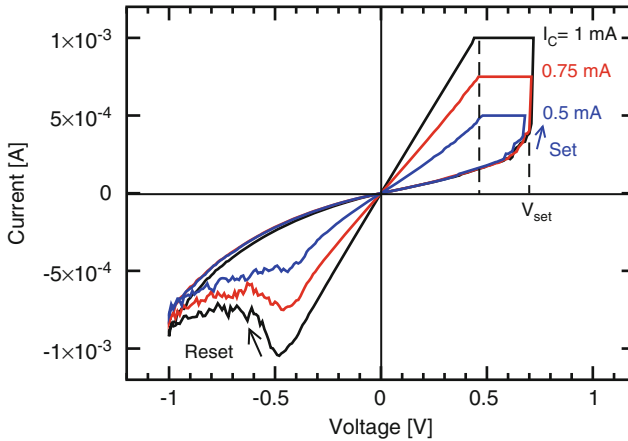
Fig. 6.4 Measured I–V characteristics for a bipolar switching RRAM, consisting of a TiN/HfO$_x$/TiN MIM stack with a 20 nm thick HfO_x layer. Set and reset take place under positive and negative polarity, respectively. Set takes place at V_{set}, then the current flowing during the set transition is externally limited to a compliance current I_C. Increasing I_C results in a decrease of the set-state resistance R and an increase of the reset current I_{reset}. Note the rather constant voltage $V_C = RI_C$ at the end of the set transition. The reset voltage V_{reset} is also almost constant and similar to V_C
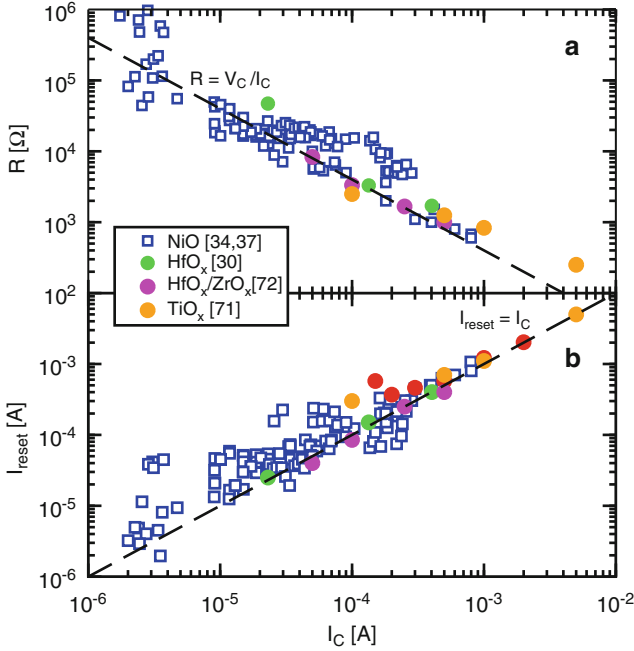
Fig. 6.5 Measured resistance R in the set state (**a**) and reset current I_{reset} (**b**) as a function of I_C, for both unipolar and bipolar switching and for several metal oxides, including NiO [21, 34, 36, 37], TiO$_x$ [71], HfO$_x$ [30], and HfO$_x$–ZrO$_x$ [72]. The resistance is inversely proportional to I_C according to Eq. (6.1), while I_{reset} is proportional to I_C according to Eq. (6.2). Note that all data follow the same universal line, irrespective of the switching mode or active material. Reprinted with permission from [45] (© 2011 IEEE)

and is thus inversely proportional to I_C given the almost constant $V_C = 0.4$ V. At negative voltage, the reset transition is initiated at a reset voltage V_{reset}, which is almost constant around 0.4 V, thus roughly equal to V_C. The reset current I_{reset} is therefore approximately given by:

$$I_{reset} = \eta I_C, \tag{6.2}$$

with $\eta \approx 1$, given that $I_{reset} = V_{reset}/R \approx V_C/R = I_C$ [61].

These findings are generally observed in most oxide-based RRAM devices, as summarized in Fig. 6.5a, b [45, 61]. Figure 6.5a, b show the measured set state resistance and the reset current, respectively, as a function of I_C under DC-mode switching. Several oxide-RRAM materials are shown in the figure, including NiO [34, 37], TiO$_x$ [71], HfO$_x$ [30], and HfO$_x$–ZrO$_x$ [72]. Data in Fig. 6.5a agree with the inverse proportionality between R and I_C in Eq. (6.1), with $V_C = 0.4$ V, while data in Fig. 6.5b confirm Eq. (6.2). The figures also report data for one transistor/one resistor (1T1R) structures, where the RRAM was in series with a MOS transistor to control the current flowing in the device during set [30, 34, 36, 37]. Data from 1T1R

devices generally feature a smaller I_{reset}, thanks to the absence of current overshoot exceeding I_C during the set transition [36, 61, 73]. Note that data in the figures align on the same trend irrespective of the active material (NiO, HfO$_x$, TiO$_x$, etc.), of the switching mode (unipolar or bipolar switching), and of the cell structure (single MIM, 1T1R device). The independence of V_C and η in Eqs. (6.1) and (6.2) on the active material suggests a *universal* switching kinetic for the formation of the CF, with little or no dependence on the metal oxide composition [45, 61].

6.4 Time-Resolved Switching Characteristics

To gain more insight into the set transition described by Eq. (6.1) and into the universal switching characteristic, where V_C does not significantly depend on the material or switching mode, time-resolved switching experiments have been carried out. In these experiments, set pulses with voltage amplitude V_A were applied to a RRAM device with a load resistance R_L in series, as illustrated in Fig. 6.6. The initial state was a reset state with resistance around 5 kΩ. A sequence of pulses with increasing pulsewidth was applied and the resistance R of the device was measured after each pulse. Between each set pulse, no reset pulse was applied, thus allowing tracking of the cumulative effect of set pulses for increasing time. The voltage across the cell during each set pulse V was also evaluated as:

$$V = \frac{R}{R + R_L} V_A, \tag{6.3}$$

where R is the resistance measured after the corresponding set pulse.

Figure 6.7 shows the measured R as a function of time for $R_L = 1$ kΩ (a), 2.2 kΩ (b) and 5 kΩ (c) and for increasing applied voltage V_A, from 1 to 3.5 V, for HfO$_x$-based RRAM devices [74]. Figure 6.7d–f show the corresponding estimated V
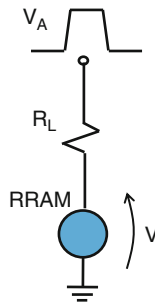
Fig. 6.6 Schematic illustration of the device layout for the time-resolved measurement of the set transition. The RRAM device is connected with a load resistance R_L to limit the current during set. A pulse with voltage V_A is applied, with a voltage drop V at the RRAM device. Reprinted with permission from [74] (©2011 IEEE)
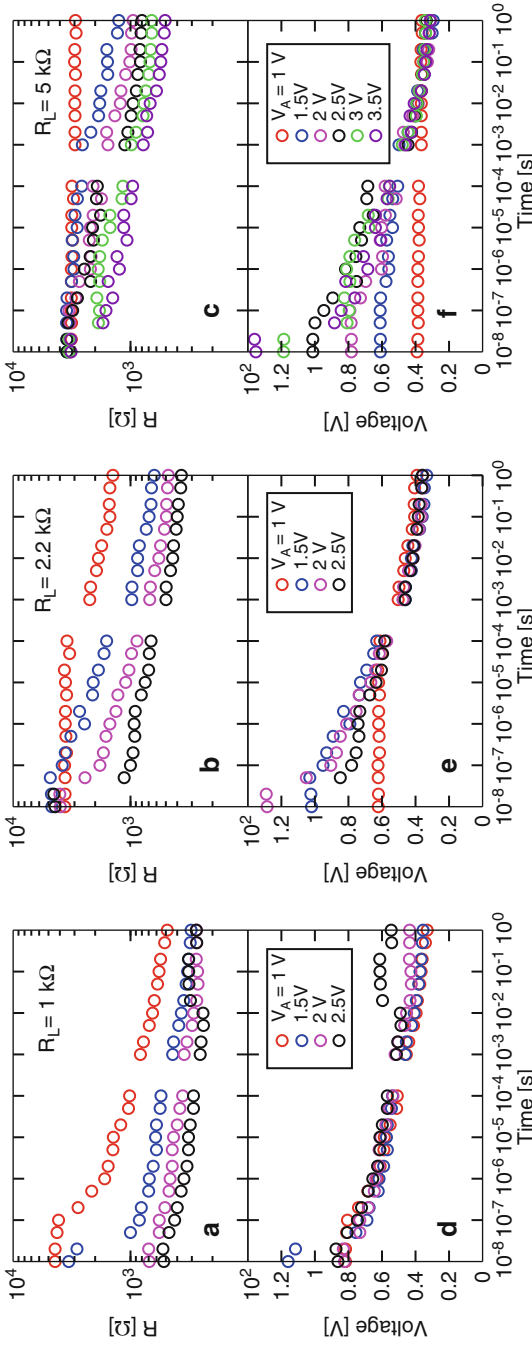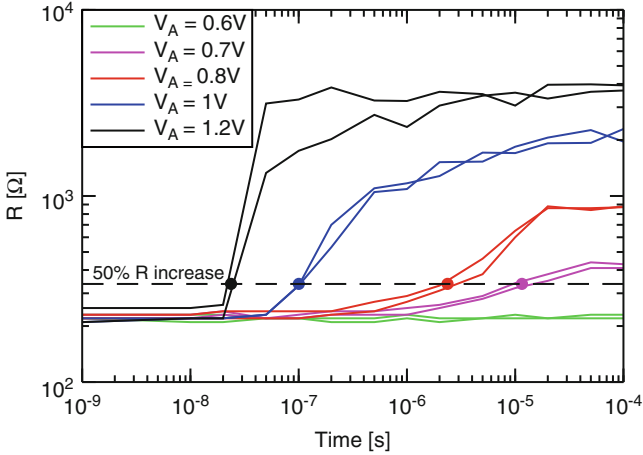
Fig. 6.7 Measured R and V for increasing load resistance R_L = 1 kΩ (**a**, **d**), 2.2 kΩ (**b**, **e**), and 5 kΩ (**c**, **f**). The resistance was measured in a broad time scale from 10 ns to 1 s at increasing V_A. The resistance drop reflects the formation and growth of the CF, where the growth rate increases for increasing V_A. The final R increases with R_L due to the decreasing compliance current. Note the universal character of the measured V across the cell, suggesting that V is the controlling parameter for the CF growth process. Reprinted with permission from [74] (© 2011 IEEE)

across the RRAM. Note the extremely wide time range in the experiments, from 100 ns to 1 s, which was possible thanks to a logarithmic increase of pulsewidth in the sequential set experiment [74]. In general, R decreases for increasing set time, as a result of the formation (nucleation) and growth of the CF. The set process becomes faster for increasing V_A, as expected due to the voltage-accelerated kinetics of filament growth. The resistance at the end of the set transient at 1 s increases for increasing R_L: This is similar to the compliance effect seen in Fig. 6.4, where a decreasing I_C (corresponding to an increase of R_L, since a larger R_L provide more limitation to the current through the device) results in a larger R at the end of set.

The resistance limitation effect in Fig. 6.7a–c can be understood by considering the time and V_A dependence of the voltage V across the cell as a function of time in Fig. 6.7d–f. Here, the RRAM voltage follows a unique function of time, which is independent from V_A and R_L. These results reveal that voltage is the controlling parameter for the filament growth process during set. In fact, V adjusts to a given value $V_C(t)$ at any time, irrespective of V_A and R_L, where V_C is dictated by the filament growth kinetics in the material. The self-adjustment of the RRAM voltage is due to the presence of a negative feedback by the presence of a load resistance in series with the cell [75]: as the CF grows, its resistance decreases, thus the voltage across the device decreases due to Eq. (6.3). The growth process thus quenches itself, resulting in a self-limiting growth kinetics. Note that, if no load resistance is put in series with the RRAM device, no negative feedback is enforced, thus leading, in principle, to an unlimited growth of the CF. (In real devices, other limitation mechanisms take place, as already demonstrated by the complementary switching behavior described in Sect. 6.3.)

The results in Fig. 6.7d–f highlight the meaning of the constant V_C at the end of the set transient in DC set experiments in Figs. 6.4 and 6.5: In particular, note in Fig. 6.7d–f that V is close to $V_C = 0.4$ V at $t = 1$ s, at the end of the set experiment. V_C has therefore the meaning of the natural voltage across the cell, which results from the CF growth in presence of a negative feedback, due, e.g., to a load resistance R_L in series with the cell in Fig. 6.7, or to a current compliance I_C in Figs. 6.4 and 6.5. Data in Fig. 6.7d–f also reveal that V_C depends on the set time, e.g., a larger V_C is expected for decreasing set time.

The universal behavior of V in Fig. 6.7d–f provides evidence for a voltage-controlled growth process in oxide-based RRAM. The voltage-controlled nature of the set transition results from the strong (e.g., exponential) dependence of the growth rate on voltage. In fact, such a strong dependence allows for a quick readjustment of the voltage across the cell at any given time during set. To gain more insight into the fundamental law governing the voltage dependence of the CF growth process, we have measured the set time t_{set} and the reset time t_{reset} as a function of cell voltage V. Set/reset times were estimated as the times for which the resistance decreases/increases by 50 % from the initial value. Figure 6.8 shows the time-resolved resistance change during reset in HfO_x RRAM, starting from a low-resistance set state and for increasing V_A between 0.6 and 1.2 V. No load resistance was applied during reset as already noted in Sect. 6.2, so that $V = V_A$. The reset time decreases for increasing V_A, revealing a similar voltage-controlled nature as evidenced for the set transition. Figure 6.9a shows the measured t_{set}/t_{reset} as a

Fig. 6.8 Measured R as a function of time during reset for increasing V_A. No load resistance was applied in series with the cell. The reset time, corresponding to a 50% increase of R, is marked on the figure, indicating an almost exponential decrease of t_{reset} for increasing voltage
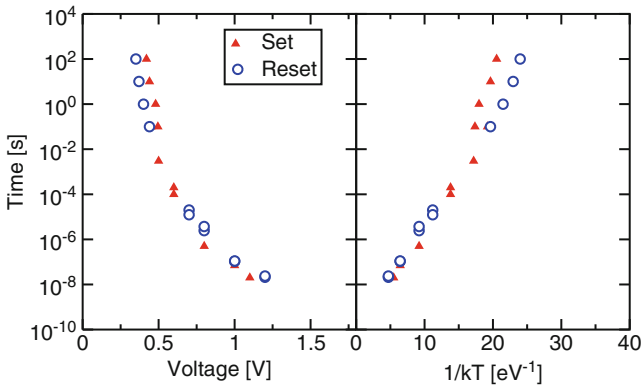
Fig. 6.9 Measured set and reset times, evaluated as a 50% resistance decrease or increase, respectively, as a function of voltage (**a**) and as a function of $1/kT$ (**b**), where T is the local temperature at the CF evaluated from the Joule heating formula of Eq. (6.4). The exponential dependence on $1/kT$ suggests that set/reset processes are due to temperature-activated mechanisms obeying an Arrhenius law

function of the cell voltage V, estimated by Eq. (6.3) with $R_L = 0$ for reset. Both t_{set} and t_{reset} follow approximately the same dependence, with a strong dependence on voltage. In fact, t_{set} and t_{reset} change by ten decades upon a voltage increase from about 0.3 V to about 1.25 V, e.g., roughly a factor 4 [74]. These results are in agreement with similar data for RRAM devices based on the migration of Ag cations [75] and based on TiO$_x$ resistive switching [3]. Note, in particular, that the t_{set} and t_{reset} does not feature an exponential behavior on voltage, thus indicating

that a simple F-model for set/reset is not sufficiently accurate. To understand the fundamental law driving set and reset kinetics, t_{set} and t_{reset} are shown in Fig. 6.9b as a function of $1/kT$, where k is the Boltzmann constant and T is the local temperature at the localized filament [74]. The local temperature was evaluated from the Joule heating model described by:

$$T = T_0 + \frac{R_{th}}{R} V^2,$$

(6.4)

where R_{th} is the effective thermal resistance at the localized CF and T_0 is the temperature of the device (i.e., room temperature) [62, 75, 76]. The thermal resistance R_{th} was evaluated as:

$$R_{th} = \frac{1}{8k_{th}} \frac{4L}{\pi\phi^2},$$

(6.5)

where k_{th} is the thermal conductivity in the CF, L is its length, assumed equal to the oxide thickness, and ϕ is the diameter of the filament, assumed to have a cylindrical shape. The factor 8 in the denominator of Eq. (6.5) is obtained by solving the Fourier differential equation in the presence of a distributed Joule dissipation [76, 77]. The electrical resistance is given by a formula similar to Eq. (6.5), except for replacing $1/(8k_{th})$ with the electrical resistivity ρ. As a result, the ratio between thermal and electrical resistance in Eq. (6.4) can be written as:

$$\frac{R_{th}}{R} = \frac{1}{8\rho k_{th}}.$$

(6.6)

For the T estimation in Fig. 6.9, a ratio $R_{th}/R = 1{,}500$ kV^{-2} was assumed, corresponding to a thermal conductivity $k_{th} = 20$ JK^{-1} cm^{-1} s^{-1}, similar to the thermal conductivity of bulk hafnium, and an electrical resistivity $\rho = 400$ μΩ cm, which is about 30 times larger than bulk hafnium value. Such a large enhancement of electrical resistivity can be understood by the nonmetallic character of the CF, generally associated with a suboxide phase such a Ti_4O_7 in the case of TiO_x RRAM [12, 13]. Also, one should consider that the electrical resistivity may be largely affected by significant surface and defect scattering at the nanoscale CF, as a result of the Fuchs–Sondheimer formula [78]:

$$\rho = \rho_{bulk} \left(1 + \frac{3}{4} \frac{\lambda}{\phi} (1 - p) \right),$$

(6.7)

where ρ_{bulk} is the bulk electrical resistivity, λ is the electron mean free path, and p is the specularity factor, namely, the probability for elastic scattering at the surface of the CF. For instance, an electrical resistivity $\rho = 380$ μΩ cm, and thus close to the value used to estimate R_{th}/R in Eq. (6.6), can be obtained for a Hf nanoscale filament of size $\phi = 1$ nm, assuming $\lambda = 28$ nm and $p = 0.5$ [61, 78]. This supports the choice of electrical resistivity in the CF.

Data for t_{set} and t_{reset} in the Arrhenius plot of Fig. 6.9b display an almost linear behavior, thus suggesting that the set/reset process for filament growth and dissolution obeys a strong temperature activation, driven by the local temperature increase due to Joule heating. Also, the similarity between t_{set} and t_{reset} suggests that set/reset mechanisms have the same nature, e.g., the temperature-activated ion migration driven by the electric field at a localized spot. The voltage application during the set/reset pulse might thus have two important roles (1) providing the necessary Joule heating to allow completion of the filament growth/dissolution in a sufficiently short time, thanks to the Arrhenius temperature activation in Fig. 6.9b, and (2) providing the necessary electric field needed to drive ion migration in the correct direction, thus allowing to either fill an existing high-resistance gap through ion migration, to nucleate and grow a CF during set, or open a high resistance gap by ion migration during reset. Note finally that set and reset times display a weak difference at small voltages and temperatures. In particular, t_{set} is generally larger than t_{reset} at small voltages, or, equivalently, the set voltage V_{set} is generally larger than the reset voltage V_{reset} for the same time scale of the set/reset experiment. This is also clear from Fig. 6.4, where V_{set} is around 0.6 V, with a smaller V_{reset} of about 0.44 V. This can be understood by the fact that set is initiated by nucleation, where the CF must be initially formed through ion migration across a high resistance gap. Such an initial condition differs significantly from the one in the reset process, starting from a continuous CF with low resistance. In particular, one may expect that the initial temperature is larger in the continuous CF with respect to the disconnected CF, as a result of the change in electrical resistance in Eq. (6.4): the relatively larger value of R in the set state, compared to the reset state, results in a smaller local temperature due to Joule heating, for the same applied voltage. In addition, one should consider that, in the set state, only the ion migration is accelerated by the temperature at the tip of the broken CF, which may be significantly smaller than the maximum temperature evaluated by Eq. (6.4). As a result, a resistance-dependent overvoltage must be supplied to the reset state to initiate the set transition. Generally, the larger the resistance, the larger the voltage needed to trigger set, according to Eq. (6.4). Note that one should also consider the change in the thermal resistance, which might possibly compensate the increase of R in Eq. (6.4). However, thermal resistance changes are believed to be less marked, due to the phonon contribution to thermal conduction in the quasi-insulating gap.

6.5   Physical Mechanism for Bipolar Switching

The previous experimental analyses have pointed out the following evidences:

- Set is a voltage-controlled process, where the filament growth kinetics is a strong function of voltage, thus the voltage across the cell follows a universal evolution with time in the presence of a load resistance or current compliance system.

- Set and reset processes share the same fundamental physical mechanism, since similar set/reset times are observed as a function of voltage across the device.
- Set and reset processes are temperature accelerated through an Arrhenius law, where the local temperature increase due to Joule heating allows for the completion of CF growth/dissolution mechanisms in an extremely short time, e.g., few ns or even sub-ns time scales.

These evidences point to a fundamental role of ion migration during set/reset processes. Ion migration, in fact, accounts for the bipolar character of switching, since ions are pushed and retracted toward one electrode during set and reset process, respectively, thus allowing for the filling and opening of a depleted gap with high resistance. Ion migration obeys also a temperature-accelerated kinetics, due to thermally activated ion hopping among localized states [61, 75, 79, 80]. In this perspective, it should be noted that Eqs. (6.1) and (6.2), which control the I_C dependence of set and reset voltage and currents, are found not only in oxide-based RRAMs (e.g., see Fig. 6.5), but also in conductive-bridge RAM (CBRAM), namely RRAM devices which rely on the migration of Ag or Cu. Such metallic ions are supplied from one of the electrodes and migrate through a high resistance layer, typically a chalcogenide glass [6, 7, 75] or an oxide layer [14, 15]. For reference, Fig. 6.10 shows the measured R (a) and the measured I_{reset} (b) as a function of I_C, for CBRAM devices based on Ag migration in GeSe and on Cu migration in SiO_x [15]. Data for HfO_x RRAM are also shown for reference [30]. Results obey Eqs. (6.1) and (6.2), although with $V_C \approx 0.2$ V and $\eta \approx 0.5$, and thus smaller than the values obtained from oxide-RRAM in Fig. 6.5. While the smaller values of V_C and η can be understood by different values of the activation energy for set and reset, the validity of Eqs. (6.1) and (6.2) suggests that the same physical mechanisms control set/reset processes in both oxide-based RRAM and CBRAM. Since the latter obviously rely on ion migration for CF formation/disruption, the same mechanisms is strongly supported as the key physical phenomenon driving set/reset in oxide-RRAM.

Figure 6.11 shows the physical picture for resistive switching in oxide-based RRAM, which is compatible with the experimental evidence gained so far. The figure shows snapshots during the set process, illustrating the nucleation (a, b) and growth (c, d) stages of the CF. The initial state corresponds to a broken CF, where conductive species (e.g., Hf ions and/or oxygen ions and/or oxygen vacancies in HfO_x) have been accumulated toward the top electrode by a previous reset process under negative voltage. The application of a positive voltage at the top electrode drives the ions toward the bottom electrode, resulting in the formation of a CF nucleus, i.e., the smallest continuous connection of the two electrodes through conductive species, and its subsequent growth. Electrical conduction through the CF results in Joule heating and a temperature increase, thus accelerating the growth process. As the filament grows, its resistance decreases, thus resulting in a decrease of the voltage across the oxide layer according to Eq. (6.3), if a compliance system or a load resistance is connected to the device during set. The resulting voltage reduction quenches the driving force for ion migration, thus slowing down the growth process. If no compliance or series resistance is present in the circuit, the
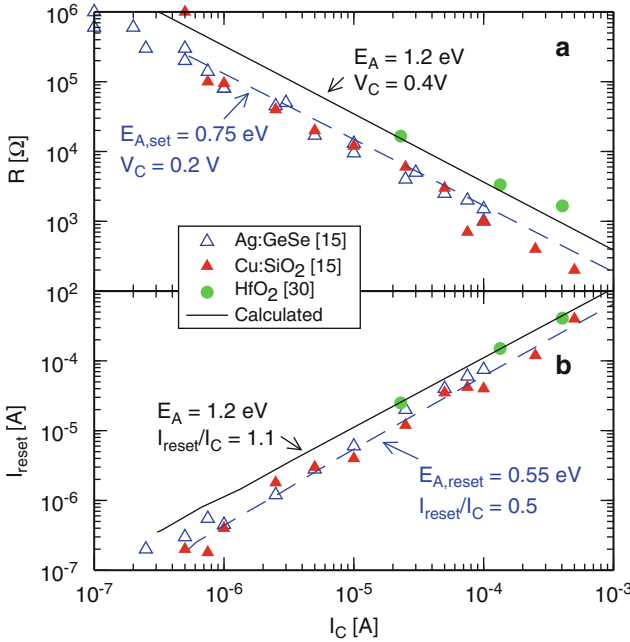
Fig. 6.10 Measured and calculated R (**a**) and I_{reset} (**b**) as a function of I_C, for HfO$_x$-based RRAM devices [30] and CBRAM devices based on Ag:GeSe or Cu:SiO$_2$ [15]. All material systems display similar behaviors in agreement with Eqs. (6.1) and (6.2), suggesting common mechanisms for set/reset in RRAM and CBRAM devices. The figure also shows calculations according to the model described in Sect. 6.6. Reprinted with permission from [74] (© 2011 IEEE)
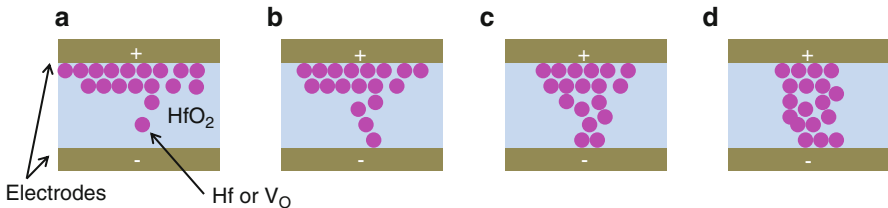
Fig. 6.11 Schematic illustration of the filamentary growth process based on ion migration during set. In a reference HfO$_2$ RRAM, ion migration results in filament nucleation (**a**, **b**) and successive growth (**c**, **d**), leading to a resistance drop during set transition. The reverse sequence applies for describing the reset process of filament dissolution. Reprinted with permission from [61] (© 2011 IEEE)

growth process will take place until all ions in the reservoir at the top electrode are used in the CF. From this point, further ion migration might result in a reduction of the CF size and in accumulation of the ions toward the bottom electrode, thus resulting in a reset process. This has been indeed demonstrated in HfO$_x$-based RRAM devices and is the basis for the complementary switching operation

described in Sect. 6.1. For an interrupted set process described by Fig. 6.11, the reset process can be described by the same sequence but in reverse order, namely from d to a.

6.6 Physical Model for Bipolar Switching

The set transition illustrated in Fig. 6.11 can be given a simple analytical description through the experimental evidence for ion migration driven by field and the local temperature [61, 74]. According to this model, the size of the CF increases with time according to the following growth equation:

$$\frac{\mathrm{d}\phi}{\mathrm{d}t} = A\mathrm{e}^{-\frac{E_A}{kT}}, \tag{6.8}$$

where E_A is the activation energy for ion migration and A is a preexponential coefficient. The model is justified by noting that the filament growth takes place through ion migration from the reservoir to the CF, and thus is limited by the migration process. The latter is thermally activated through the Arrhenius law, as already evidenced from experiments shown in Fig. 6.9. From this perspective, A may be a rather complicated function of ion diffusivity in the considered active oxide or grain boundaries, the filament length L, and the composition/volume of the ion reservoir (pure metallic phase, oxygen deficient oxide, etc.). The local temperature T in Eq. (6.8) can be obtained by the Joule heating in Eq. (6.4), while the activation energy decreases due to the applied field as a result of the barrier lowering effect. This is shown in Fig. 6.12, where the potential profile along the
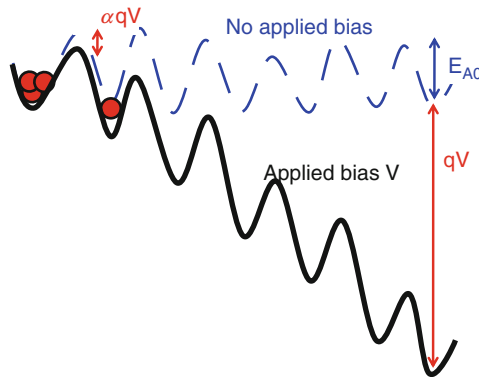
Fig. 6.12 Schematic illustration of the voltage-induced lowering of the energy barrier for ion hopping during filamentary growth/dissolution. Ions hop among potential wells through thermal excitation over potential barriers of amplitude E_{A0}. The voltage V lowers the barrier by an amount $q\alpha V$, thus enhancing migration in the direction of the electric field. Reprinted with permission from [45] (© 2011 IEEE)

active oxide layer is depicted for zero and nonzero applied voltages [45, 75]. Application of a voltage V across the oxide layer results in a lowering of the barrier according to:

$$E_A = E_{A0} - q\alpha V, \tag{6.9}$$

where E_{A0} is the zero-field activation energy and α is a constant [45, 75]. Substitution of Eqs. (6.4) and (6.9) in Eq. (6.8) results in:

$$\frac{d\phi}{dt} = A e^{-\frac{E_{A0} - q\alpha V}{k(T_0 + R_{th}/RV^2)}}, \tag{6.10}$$

which shows that application of a voltage has two enhancement effects on the growth rate, namely the barrier lowering and the Joule heating. Note that, while the model fully describes the growth process, it cannot account for the nucleation process, where the initial high-resistance gap is filled by ions. However, this approximation is largely acceptable because (1) the nucleation process only results in a minor overvoltage of V_{set} with respect to V_{reset}, of about $V_{set} - V_{reset} = 0.15$ V in Fig. 6.9, and (2) the correlation between R and I_C in Fig. 6.5a depends on the latest steps of the filament evolution, largely in the growth regime when the model in Eq. (6.10) already applies. Therefore, to understand and account for the set/reset characteristics in Figs. 6.5 and 6.7, the growth model provides sufficient physical accuracy.

The reset process can be modeled by Eq. (6.10) with a simple change in the sign of the preexponential coefficient A, to describe a decrease in size of the CF, instead of a growth. Such a reset model fully accounts for the Joule heating and filament evolution in the initial stages of the reset process, when there is a continuous CF connecting the two electrodes. On the other hand, the model may fail in describing the later stages of reset, when the gap opening results in a change in the thermal and electrical description of the filament. However, the model fully accounts for the calculation of parameters V_{reset} and I_{reset} in Fig. 6.5b, which are responsible for the initiation of the reset process.

6.7   Simulation Results

Figure 6.13 shows measured and calculated resistance and voltage across the cell for different load resistance $R_L = 1$ kΩ (a, d), 2.2 kΩ (b, e), 5 kΩ (c, f). Data are the same as in Fig. 6.7, while calculations were performed with Eq. (6.10) assuming $E_A = 1.2$ eV, $A = 1$ ms^{-1} and $\alpha = 0.3$ [74]. The value chosen for the activation energy is in agreement with the energy barrier for diffusion and migration observed in various oxide systems, including NiO [62, 63, 76] and Gd-doped MoO [80]. Such a value should be viewed as the energy barrier for ion migration according to the schematic of Fig. 6.12. The value used for the barrier lowering coefficient α is
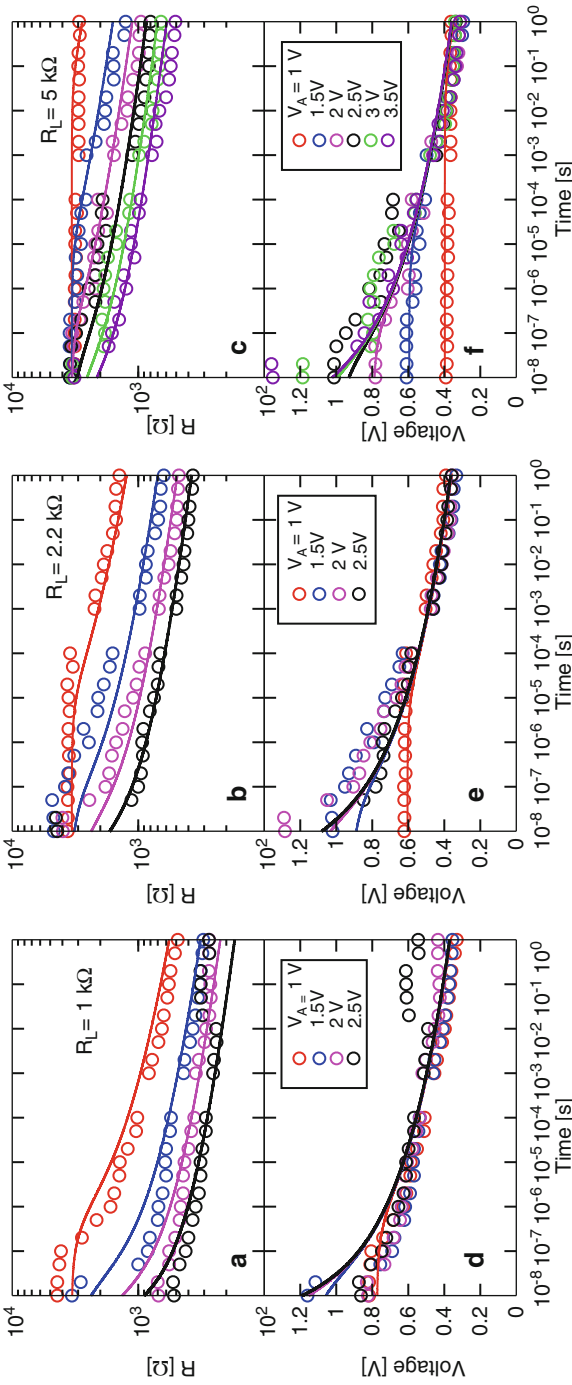
Fig. 6.13 Measured and calculated R and V for increasing load resistance $R_L = 1$ kΩ (**a, d**), 2.2 kΩ (**b, e**), and 5 kΩ (**c, f**). Calculations were performed using Eq. (6.10) with parameters $E_{A0} = 1.4$ eV, $\alpha = 0.3$, and $A = 1$ m s^{-1}. The model accounts for (1) the voltage acceleration of filament growth, (2) the dependence on R_L due to current limitation, and (3) the universal time evolution of V, due to the exponential dependence of filament growth on V. Reprinted with permission from [74] (© 2011 IEEE)
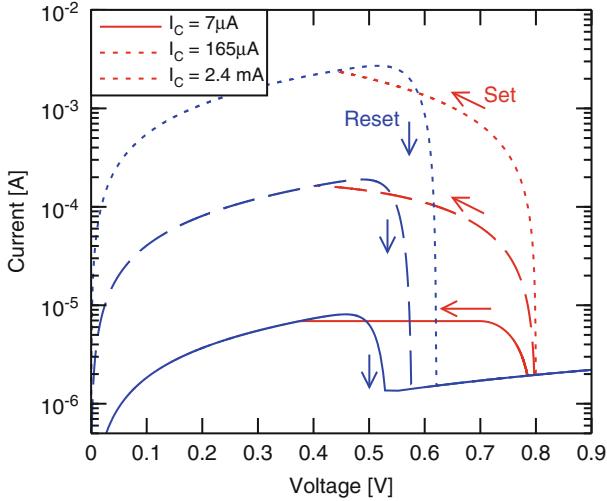
Fig. 6.14 Calculated *I–V* characteristics for set and reset at increasing $I_C = 7$ µA, 165 µA, and 2.4 mA. A 1T1R structure was assumed in the calculations, with a constant applied voltage $V_A = 0.8$ V during set and a voltage sweep during reset. Reprinted with permission from [61] (© 2011 IEEE)

similar to previous analysis [75, 79]. The choice of each of these values will be later sustained by individual comparisons with data. The calculations in the figure account very well for experimental data, in terms of voltage acceleration of the set process, where the increase of V_A results in an increase of the growth speed revealed by the decrease of the resistance, and of the compliance effect, where the increase of R_L results in a stronger limitation of the current, thus limiting the final size of the CF. In particular, note that the model accounts for the universal dependence of *V* on *t* in Fig. 6.13d–f, irrespective of the applied voltage and load resistance. This is because the growth rate in Eq. (6.10) is a strong function of *V*, thus enabling a regulation of the voltage across to the device thanks to the negative feedback loop, where any filament growth results in a decrease of voltage.

Figure 6.14 shows the calculated *I–V* curve during set and reset for increasing values of $I_C = 7$ µA, 166 µA and 2.4 mA. Simulations were performed assuming a 1T1R structure, where the saturated current in the MOS transistor was given by $I_{sat} = KV_{OD}^2/2$, with $K = 700$ µA cm^{-2}. V_{OD} represents the overdrive voltage, namely, the gate voltage minus the threshold voltage of the MOS transistor. The current compliance is thus given by the saturated MOS current and was changed in the simulations by changing the gate voltage at the MOS transistor. A voltage $V_A = 0.8$ V was applied during set from a reset state consisting of a high resistance state with an initial filament of $\phi_N = 0.5$ nm diameter. During set, the current increases due to filament growth and the consequent decrease of resistance. Once the saturated current is approached, the voltage across the device decreases similar to Eq. (6.3) (although no load resistance can properly be defined in the case of
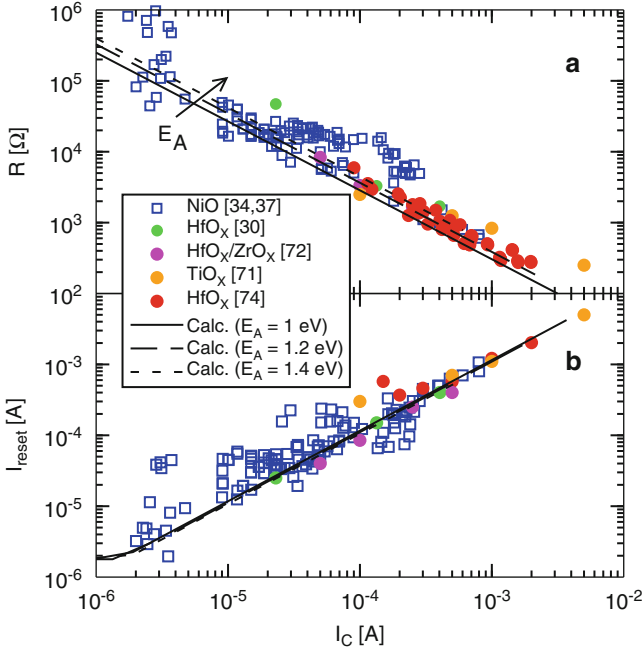
Fig. 6.15 Measured and calculated R in the set state (**a**) and reset current I_{reset} (**b**) as a function of I_C, for both unipolar and bipolar switching and for several metal oxides, including NiO [21, 34, 36, 37], TiO$_x$ [71], HfO$_x$ [30, 74], and HfO$_x$–ZrO$_x$ [72]. Calculations by the filament growth model accounts for Eqs. (6.1) and (6.2) describing the I_C dependence of R and I_{reset}, respectively. The constant voltage V_C is due to the voltage regulation effect during set under a limited current compliance, as shown in Figs. 6.13 and 6.14. The similar values for I_{reset} and I_C are due to the common nature of set and reset mechanisms, driven by the same activation energy E_{A0}. The universal R and I_{reset} behaviors are due to the weak dependence on E_{A0}, as shown by calculations for variable energy barrier. Reprinted with permission from [61] (© 2011 IEEE)

nonlinear MOS characteristics). After 1 s, which was the maximum set time in the calculation, the voltage reached a value V_C of about 0.4 V, and thus the final resistance obeys Eq. (6.1). During reset the MOS transistor was biased to a large conductivity to allow negligible series resistance in the 1T1R. The device current increases according to the I–V curves in the final set state until reset takes place at V_{reset}, which is slightly larger than V_C. As a result, the reset current I_{reset} is only slightly larger than I_C, thus satisfying Eq. (6.2). Note the abrupt current drop in the calculations, which is due to the rapid decrease of CF size and the consequent increase of resistance as the temperature reaches the critical value for the onset of ion migration.

Figure 6.15 shows the measured and calculated R (a) and I_{reset} (b) as a function of I_C, for several oxide-based RRAM in the literature [21, 30, 34, 36, 37, 71, 72]. Calculations were done assuming a total time of 1 s during set and a sweep rate of 2 V s^{-1} during reset, corresponding to DC switching. Calculations in Fig. 6.15a, b

satisfy Eqs. (6.1) and (6.2), respectively, for set and reset, as a result of the voltage-controlled set/reset kinetics. Calculations were done at variable $E_A = 0.9$, 1.2 and 1.5 eV, while A and α were kept unchanged. A decrease of E_A leads to a weak decrease in V_C: This is because the energy barrier decreases enhances ion migration, thus a lower temperature (hence voltage) is needed to sustain filament growth at any given time. The voltage thus readjusts to a smaller value during set under the negative feedback condition of Eq. (6.3). However, the change of V_C is relatively small, about 0.03 V for a 0.1 eV change of E_A in the range considered. Such a small sensitivity of set characteristic to E_A might explain why most oxide materials display the same V_C in Fig. 6.15a. Note also that the similarity between I_{reset} and I_C, namely $\eta \approx 1$ in Eq. (6.2), can be attributed to the fact that set and reset processes rely on the same physical mechanism, namely temperature and field activated ion migration. This ensures that the same voltage (hence temperature) is needed to activate migration during either set or reset, irrespective of the polarity, thus causing $V_{reset} = V_C$. As a consequence, the reset I_{reset} is also approximately equal to I_C, as already stated in Eq. (6.2) where $\eta \approx 1$.

To better understand the set mechanism, and in particular the universal time evolution of the voltage across the cell during set, one may consider rewriting Eq. (6.10) in the following way:

$$dt = A^{-1}d\phi e^{\frac{E_A}{k(T_0+R_{th}/RV^2)}} = A^{-1}d\phi e^{\frac{E_A}{kT_0\left(1+\beta I_C^2/\phi^4\right)}}, \tag{6.11}$$

where E_A has been assumed a constant for simplicity, an ideal current limitation to a constant $I_C = V/R$ was considered and the parameter β has been introduced, given by:

$$\beta = \frac{2\rho L^2}{\pi^2 k_{th} T_0}. \tag{6.12}$$

The integration of Eq. (6.11) leads to:

$$t_P = \int_{\phi_N}^{\phi_{set}} d\phi A^{-1} e^{\frac{E_A}{kT_0\left(1+\beta I_C^2/\phi^4\right)}} = \int_{\phi_N}^{\phi_{set}} f(\phi)d\phi, \tag{6.13}$$

where t_P is the total duration of the set pulse, $f(\phi)$ is the function within the integral, and ϕ_{set} is the final diameter of the filament at the end of the set transition. The function $f(\phi)$ in Eq. (6.13) cannot be integrated analytically. Figure 6.16 shows the calculated function f as a function of ϕ (a) and the corresponding integral, namely the duration of the set time (b), for three values of the current compliance $I_C = 1$, 10 and 100 μA. Both ϕ and its integral are steeply increasing functions of the diameter, which indicates that the filament growth under constant I_C extends over several decades of time with relatively little increase of diameter. The integral of Eq. (6.13) can be found by interpolation of the calculated curves at the total set time t_P, and the
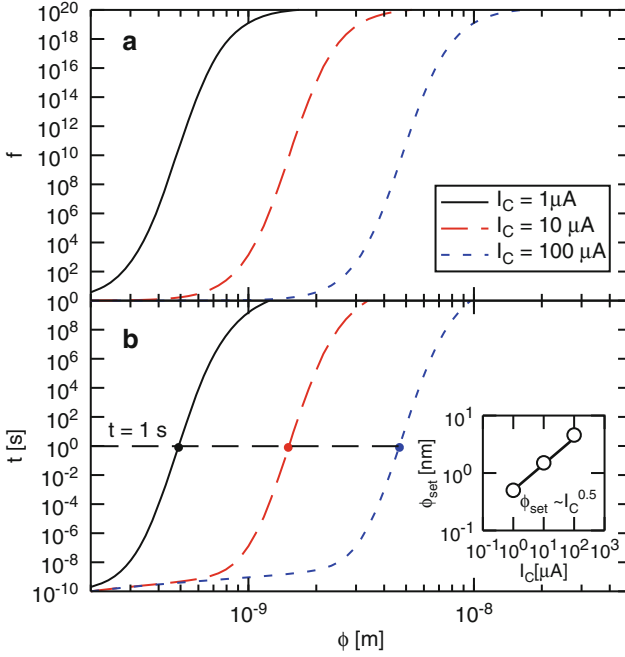
Fig. 6.16 Calculated function f in the integral of Eq. (6.13) (**a**) and time t resulting from the integration of the same equation (**b**) for increasing $I_C = 1$, 10, and 100 µA. The *curves* of calculated t for a set time $t_P = 1$ s indicate the final filament size after set transition, as shown in the *inset* as a function of I_C. The proportionality $\phi_{set} \propto I_C^{0.5}$ is consistent with $R \propto I_C^{-1}$, thus providing a physical basis for the empirical formula in Eq. (6.1)

result is shown for $t_P = 1$ s, corresponding to a typical DC switching experiment. In all cases, the resulting ϕ_{set} is found in the steep region of the integral of Fig. 6.16b. From inspection of Eq. (6.13), one may expect that the condition $t_P = 1$ s is satisfied by a critical value of the term $C^2 = \beta I_C^2/\phi^4$ in the denominator of the exponent. This is demonstrated by the inset of Fig. 6.16, showing the extracted ϕ_{set} as a function of I_C and showing that ϕ_{set} is proportional to $I_C^{0.5}$. Note that latter can be viewed as $R \propto \phi^{-2} \propto I_C^{-1}$, namely Eq. (6.1). The physical meaning of the parameter $C = \beta^{0.5} I_C/\phi^2$ controlling the exponent in the integral of Eq. (6.13) can be understood by a simple elaboration, showing that:

$$C = \frac{\beta^{0.5} I_C}{\phi^2} = \frac{RI_C}{\sqrt{2k_{th}\rho T_0}} = \frac{V}{\sqrt{2k_{th}\rho T_0}}, \qquad (6.14)$$

namely C is proportional to V through a constant $(2k_{th}\rho T_0)^{-1}$. Therefore, Eq. (6.13) indicates that there is a correspondence between V across the cell and time during the set transition. This is shown in Fig. 6.17, showing $C \propto V$ as a function of time for the three values of I_C in Fig. 6.16: C (hence V) follows a universal function of time, irrespective of the current compliance, in agreement with results shown in Fig. 6.13.

Fig. 6.17 Calculated
parameter $C = \beta^{0.5} I_C \phi^{-2}$ as a
function of time according
to Eq. (6.14), for increasing
I_C. The independence from
I_C accounts for the universal
time evolution of voltage in
Fig. 6.13
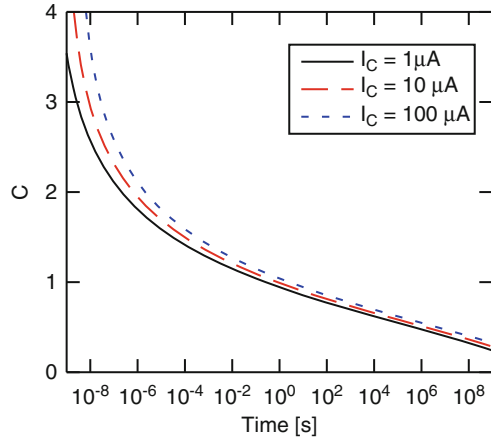
6.8 Switching Time and Energy

Switching speed and switching energy are among the most important properties
defining the performance of a new device for low power, high speed integrated
circuits. Figure 6.18 shows the calculated reset time t_{reset} as a function of V (a) and
as a function of $1/kT$ (b). The figure also shows experimental data for set and reset
times (same data as in Fig. 6.9). The same parameter values for E_A, A, and α in
Fig. 6.13 were used, while three different CF sizes were used, corresponding to
$R = 220\ \Omega$, 10 kΩ, and 400 kΩ. The model accounts very well for the switching
times in both the voltage and Arrhenius plots. In particular, the Arrhenius behavior,
which is a key feature in the filament growth model, is clearly indicated by data
aligning on a straight line in Fig. 6.13b. A more detailed analysis reveals that the
data and calculations in Fig. 6.13b are slightly nonlinear: this can be understood by
the voltage-induced barrier lowering, which results in a decrease of E_A (i.e., a
flattening of the curve in the Arrhenius plot) for increasing voltage, hence decreas-
ing $1/kT$. These results also provide a direct way to extract the microscopic
parameters for ion migration from experimental data, namely the activation energy
E_A can be extracted from the slope of data in the Arrhenius plot and the barrier
lowering coefficient α can be extracted from the curvature of data in the Arrhenius
pot. The figure also compares calculations for different initial sizes of the filament,
showing that a smaller CF requires a shorter time for reset. Given the symmetry
between set and reset, the same conclusion might be drawn for the set transition,
provided that set is conducted at constant voltage as assumed for reset in Fig. 6.13.
No dependence on final filament size is instead expected when variable CF sizes are
achieved through different compliance levels, such as in Figs. 6.4 and 6.7. A
reduction of set/reset times by roughly a factor 40 is expected for an increase of
resistance from 220 Ω to 400 kΩ. This factor reflects the difference in the initial
diameter ϕ_{set} of the filament, which can be estimated as $(400\ \mathrm{k}\Omega/220\ \Omega)^{0.5} \approx 40$.
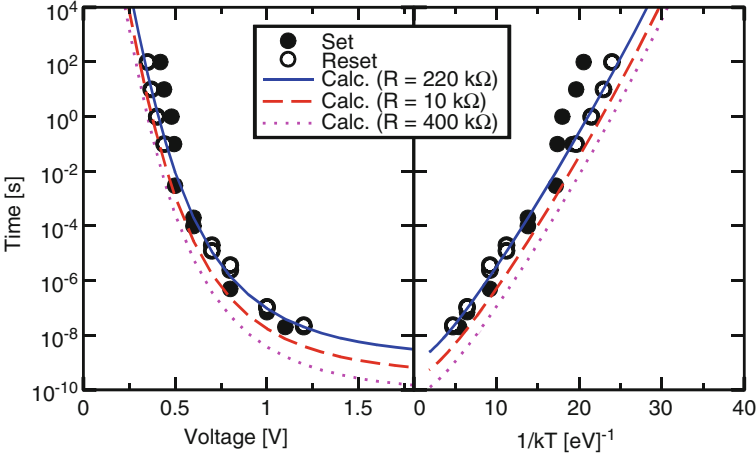
Fig. 6.18 Measured set and reset times, as a function of V (**a**) and $1/kT$ (**b**), where T is the local temperature at the switching location. Calculations of the reset time are also shown for increasing $R = 220\ \Omega$, $10\ k\Omega$, and $400\ k\Omega$. Note that the curve in the Arrhenius plot is not perfectly linear, as a result of the voltage-induced energy barrier lowering. Adapted from [74] (© 2011 IEEE)

In fact, according to the filament growth model, the reset time can be given by the formula [76]:

$$t_{\text{reset}} = \frac{\phi_{\text{set}}}{2v_{\text{G}}}, \tag{6.15}$$

where v_G is an effective growth velocity. Eq. (6.15) indicates that, for any given voltage, the reset time should be proportional to the initial filament size ϕ_{set}.

Figure 6.19 shows the calculated reset energy E_{reset} as a function of voltage for the three resistance values used in Fig. 6.18. Data for an initial resistance of 220 Ω are also shown for reference. The energy was calculated by the integral:

$$E_{\text{reset}} = \int_{\text{reset}} VI\,\mathrm{d}t = \int_{\text{reset}} \frac{V^2}{R}\,\mathrm{d}t, \tag{6.16}$$

that is the integral of dissipated power in time during the reset transition. Note that only the energy dissipation in the device is considered in Eq. (6.16), while more energy could be dissipated at the series transistor/resistance or at the select device. The set energy E_{set} dissipated in the device is equal to E_{reset} for a constant voltage set, since set is just a reversed reset process in this case. For an I_C-controlled set, such as in Fig. 6.14, the E_{set} is expected to be even smaller than E_{reset}, because, although V could be higher to provide the nucleation overvoltage, the transition becomes faster at high voltage according to the exponential relationship in Eq. (6.10), therefore reducing the product $V^2\mathrm{d}t$ in Eq. (6.16).

Fig. 6.19 Measured and
calculated set/reset energy as
a function of V for
$R = 220\ \Omega$, $10\ k\Omega$, and
$400\ k\Omega$. The energy largely
decreases for increasing V,
due to the switching times
decreasing almost
exponentially in Fig. 6.18,
and for increasing R, as a
result of the decreasing I in
Eq. (6.16). Adapted from [74]
(© 2011 IEEE)
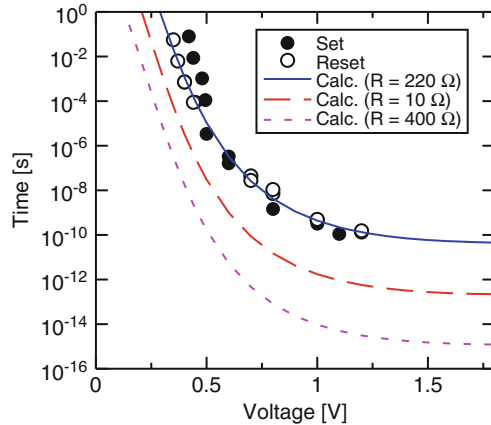
Results in Fig. 6.19 suggest two ways to efficiently reduce the reset energy in RRAM: First, E_{reset} decreases significantly for increasing voltage, as a result of the almost exponential enhancement of transition speed with voltage in Eq. (6.10). Second and most importantly, reducing the size of the CF results in a remarkable reduction of E_{reset} at a given voltage, thanks to the increase of R in Eq. (6.16). From the figure, reset energies of the order of 10 fJ can be achieved by reset at about 1 V on a RRAM device with $400\ k\Omega$ resistance, corresponding to 2.5 µA reset current and 5 ns switching.

6.9   Scaling Challenges

From the results in Figs. 6.18 and 6.19, CF size control and reduction appears as an effective way to reduce both transition time and energy consumption in RRAM. To achieve such large CF resistances, however, one should ensure a sufficiently high resistance in the reset state, too. In this perspective, having a large resistance window available in the RRAM device is a key requirement, since it allows writing extremely small CFs by taking advantage of the improved programming speed and reduced energy consumption.

The reduction of the CF size has another important impact on the scaling of memory arrays with crossbar architecture. In fact, one of the most attractive features of RRAM is the ability to organize the memory array in a crossbar circuit, where each memory cell occupies an area of only $4F^2$ [4, 50, 54]. However, such architecture is prone to interference during program and read. For instance, application of a voltage across a cell during read results in a sneak-through current through cell belonging to the same row or column: this may result in a major misinterpretation of the bit status, when the cell to be read is in the high resistance state [44, 49, 50]. To solve this issue, each memory cell must be accompanied by a nonlinear selector, e.g., a rectifier diode [49–51]. Several types of select devices
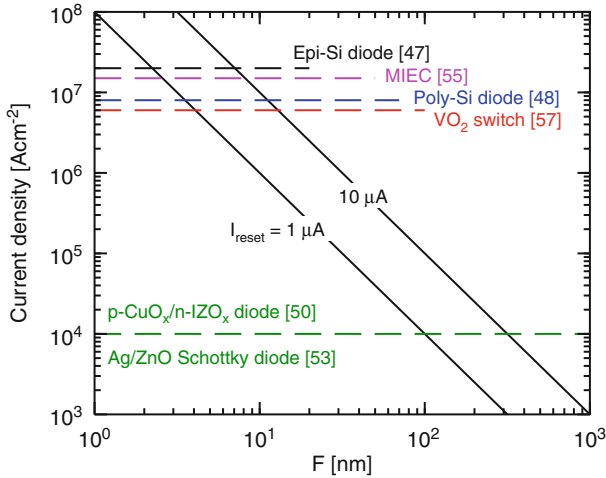
Fig. 6.20 Reset current density as a function of the technology node F, assuming a constant reset current $I_{reset} = 1$ and $10\,\mu A$. The reset current increases for decreasing F according to $I_{reset} \propto F^{-2}$. The current density reported in literature for Si and non-Si diodes is also shown for comparison [47–53, 55, 56]. Reprinted with permission from [37] (© 2011 Elsevier, Ltd.)

have been proposed so far, including monocrystalline silicon diodes [47], polycrystalline silicon diodes [48], oxide unipolar heterostructure diodes [49–52], Schottky diodes [53], mixed ionic–electronic conduction diodes [55, 56], and VO_2 threshold switches [51, 57]. For the purpose of diode screening for selector applications, three critical requirements should be considered: First, the diode should be available in the back-end of the line, to allow the stacking of several memory layers. Si-based selectors may hardly be compatible with such requirement due to the high temperatures needed for deposition and doping diffusion/activation. The second key requirement is a sufficient ON/OFF current ratio of the selector, to allow for sufficient blocking of the current through unselected devices during read. Finally, an important requirement is the capability to supply sufficient current during program, to allow for the set/reset of the memory element. Such a requirement seems the most hard to be met: Fig. 6.20 shows the current density at about 2 V of reported select elements, compared to the reset current density as a function of the device size F [37]. Note that the required current density increases for decreasing F, and thus with the down scaling of the memory cell. Therefore, to meet the reset current requirement in future technology nodes, one should ensure (1) satisfactory current density in the select element and (2) sufficiently small reset current $I_{reset} = V_{reset}/R$, and thus sufficiently small CFs. From this standpoint, the size reduction of filaments in oxide RRAM is essential.

In view of CF scaling, it should also be mentioned that CF size reduction might conflict with reliability requirements, namely data retention and noise issues. Data retention at elevated temperature was in fact shown to strongly depend on the CF
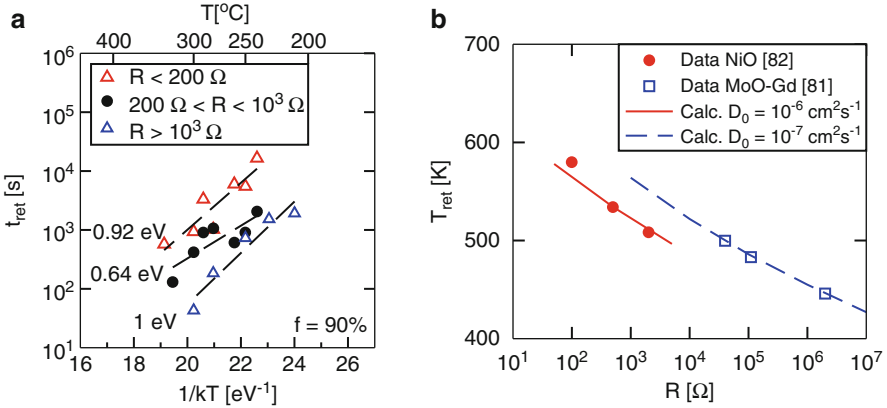
Fig. 6.21 Measured retention times at 10 % percentile [81] (**a**) and measured/calculated retention temperatures as a function of initial resistance [80, 81] (**b**). Three different initial resistances were used in (**a**), namely less than 200 Ω, between 200 and 1,000 Ω, and above 1,000 Ω. The retention times obey the Arrhenius law, however t_{ret} decreases for increasing R, as a result of size-dependent oxidation [81]. The retention temperature change at 1,000 s can be reproduced by the analytical reset model of Eq. (6.18). Reprinted with permission from [81] and [82] (© 2011 IEEE and ECS)

resistance, since smaller filaments with higher resistances were found to display shorter retention time according to the formula [80, 81]:

$$t_{ret} = \frac{\phi_{set}^2}{D_0} e^{\frac{E_A}{kT}} \qquad (6.17)$$

where D_0 is a diffusivity factor. Equation (6.17) is based on a diffusion model, where the diffusion of conductive atoms from a CF is driven by the concentration gradient, and thus critically depends on CF size [77]. Figure 6.21a shows the Arrhenius plot of retention times for a failure rate of 10 %, i.e., the retention time of one device out of 10 devices on the average was shorter than t_{ret} in the figure. Data are reported for a cell initially programmed within three different resistance ranges, namely below 200 Ω, between 200 Ω and 1 kΩ, and above 1 kΩ. Data retention time decreases for increasing resistance, and thus decreasing size of the CF. Figure 6.21b shows the retention temperature corresponding to $t_{ret} = 10^3$ s as a function of initial resistance, from Fig. 6.21a [82] and from MoO-Gd RRAM devices [80]. The retention temperature T_{ret} decreases with R according to the formula:

$$T_{ret} = \frac{E_A}{k \log \frac{D_0 t_{ret}}{\phi_{set}^2}} \approx \frac{E_A}{k \log \frac{\pi R D_0 t_{ret}}{4\rho L}}, \qquad (6.18)$$

where the ohmic approximation for R was used. Calculations based on Eq. (6.17) are also shown in the figure, supporting the size-dependent retention model.

Another potential concern for small CFs is the fluctuation of the current during read, which might be induced by surface charging/discharging effects due to surface rearrangement [83]. The relative amplitude of random telegraph noise (RTN) has been shown to increase for decreasing CF size, as a result of the stronger impact of surface conduction [83]. From this viewpoint, the trade-off between reset time/energy reduction and reliability must be carefully assessed.

6.10 Conclusions and Outlook

RRAM is the strongest candidate for high-density nonvolatile memory technologies below the 10 nm node. The RRAM technology offers several key advantages, such as switching speed, low voltage operation, good retention and endurance reliability, and low cost. However, the scalability of RRAM is still under debate, due to the lack of understanding and physically based models for the switching mechanisms. This review provides an overview of the recent progress on the physical interpretation and modeling of the oxide-based bipolar switching RRAM. The switching mechanism has been discussed based on experimental results regarding the time evolution of resistance and voltage across the cell, revealing the key role of voltage as the controlling parameter for the switching characteristic. The voltage dependence of switching times has provided evidence for an Arrhenius law, revealing the temperature-activated nature of the switching process and the key role of voltage-driven Joule heating at the localized filament. It has been thus concluded that set/reset processes of bipolar switching RRAM rely on thermally activated ion migration driven by the electric field. Based on this physical interpretation, a model has been developed to describe the filament growth and dissolution during set and reset, respectively. The filament grows/dissolves through ion migration in the direction of the field, and such process is strongly accelerated by the local temperature, which largely increases through Joule heating. The model was tested against the time dependence of set dynamics, the set/reset parameters as a function of current compliance, and the set/reset times. Finally, the consequences of this new understanding and modeling in terms of scaling have been discussed. In particular, RRAM technology will face a severe challenge in matching, on the one hand the requirement of reducing time, energy, and space within the chip (i.e., cost), and, on the other hand, the current density limits of select devices and size-dependent reliability issues of the RRAM device.

References

1. R. Waser, M. Aono, Nanoionics-based resistive switching memories. Nat. Mater. **6**, 833–840 (2007)
2. A. Sawa, Resistive switching in transition metal oxides. Mater. Today **11**, 28–36 (2008)
3. R. Waser, R. Dittmann, G. Staikov, K. Szot, Redox-based resistive switching memories—nanoionic mechanisms, prospects, and challenges. Adv. Mater. **21**, 2632–2663 (2009)
4. D. Ielmini, R. Bruchhaus, R. Waser, Thermochemical resistive switching: Materials, mechanisms and scaling projections. Phase Transit. **84**, 570–602 (2011)
5. H. Akinaga, H. Shima, Resistive random access memory (ReRAM) based on metal oxides. Proc. IEEE **98**, 2237–2251 (2010)
6. M.N. Kozicki, M. Park, M. Mitkova, Nanoscale memory elements based on solid-state electrolytes. IEEE Trans. Nanotechnol. **4**, 331–338 (2005)
7. M. Kund, G. Beitel, C.-U. Pinnow, T. Rohr, J. Schumann, R. Symanczyk, K. Ufert, G. Muller, Conductive bridging RAM (CBRAM): An emerging non-volatile memory technology scalable to sub 20 nm. IEDM Tech. Dig. 754–757 (2005)
8. S. Lombardo, J.H. Stathis, B.P. Linder, K.L. Pey, F. Palumbo, C.H. Tung, Dielectric breakdown mechanisms in gate oxides. J. Appl. Phys. **98**, 121301 (2005)
9. X. Li, C.H. Tung, K.L. Pey, The nature of dielectric breakdown. Appl. Phys. Lett. **93**, 072903 (2008)
10. X. Li, C.H. Tung, K.L. Pey, V.L. Lo, The chemistry of gate dielectric breakdown. IEDM Tech. Dig. 779–782 (2008)
11. G.-S. Park, X.-S. Li, D.-C. Kim, R.-J. Jung, M.-J. Lee, S. Seo, Observation of electric-field induced Ni filament channels in polycrystalline NiO_x film. Appl. Phys. Lett. **91**, 222103 (2007)
12. D.-H. Kwon, K.M. Kim, J.H. Jang, J.M. Jeon, M.H. Lee, G.H. Kim, X.-S. Li, G.-S. Park, B. Lee, S. Han, M. Kim, C.S. Hwang, Atomic structure of conducting nanofilaments in TiO_2 resistive switching memory. Nat. Nanotechnol. **5**, 148–153 (2010)
13. J.P. Strachan, M.D. Pickett, J.J. Yang, S. Aloni, A.L.D. Kilcoyne, G. Medeiros-Ribeiro, R.S. Williams, Direct identification of the conducting channels in a functioning memristive device. Adv. Mater. **22**, 3573 (2010)
14. C. Schindler, S.C.P. Thermadam, R. Waser, M.N. Kozicki, Bipolar and unipolar resistive switching in Cu-doped SiO_2. IEEE Trans. Electron Devices **54**, 2762–2768 (2007)
15. C. Schindler, Resistive switching in electrochemical metallization memory cells. PhD Thesis, Rheinisch-Westfalischen Technischen Hochschule Aachen, 2009
16. J.F. Gibbons, W.E. Beadle, Switching properties of thin NiO films. Solid State Electron. **7**, 785–790 (1964)
17. F. Argall, Switching phenomena in titanium oxide thin films. Solid State Electron. **11**, 535–541 (1968)
18. W.R. Hiatt, T.W. Hickmott, Bistable switching in niobium oxide diodes. Appl. Phys. Lett. **6**, 106–108 (1965)
19. A. Beck, J.G. Bednorz, C. Gerber, C. Rossel, D. Widmer, Reproducible switching effect in thin oxide films for memory applications. Appl. Phys. Lett. **77**, 139–141 (2000)
20. Y. Watanabe, J.G. Bednorz, A. Bietsch, C. Gerber, D. Widmer, A. Beck, S.J. Wind, Current-driven insulator–conductor transition and nonvolatile memory in chromium-doped $SrTiO_3$ single crystals. Appl. Phys. Lett. **78**, 3738–3740 (2001)
21. S. Seo, M.J. Lee, D.H. Seo, E.J. Jeoung, D.-S. Suh, Y.S. Joung, I.K. Yoo, I.R. Hwang, S.H. Kim, I.S. Byun, J.-S. Kim, J.S. Choi, B.H. Park, Reproducible resistance switching in polycrystalline NiO films. Appl. Phys. Lett. **85**, 5655–5657 (2004)
22. I.G. Baek, M.S. Lee, S. Seo, M.J. Lee, D.H. Seo, D.-S. Suh, J.C. Park, S.O. Park, H.S. Kim, I.K. Yoo, U.-I. Chung, J.T. Moon, Highly scalable nonvolatile resistive memory using simple binary oxide driven by asymmetric unipolar voltage pulses. IEDM Tech. Dig. 587–590 (2004)
23. S.R. Lee, K. Char, D.C. Kim, R. Jung, S. Seo, X.S. Li, G.-S. Park, I.K. Yoo, Resistive memory switching in epitaxially grown NiO. Appl. Phys. Lett. **91**, 202115 (2007)

24. H. Shima, F. Takano, H. Akinaga, Resistance switching in the metal deficient-type oxides: NiO and CoO. Appl. Phys. Lett. **91**, 012901 (2007)
25. B.J. Choi, D.S. Jeong, S.K. Kim, C. Rohde, S. Choi, J.H. Oh, H.J. Kim, C.S. Hwang, K. Szot, R. Waser, B. Reichenberg, S. Tiedke, Resistive switching mechanism of TiO_2 thin films grown by atomic-layer deposition. J. Appl. Phys. **98**, 033715 (2005)
26. D.B. Strukov, G.S. Snider, D.R. Stewart, R.S. Williams, Nature **443**, 80–83 (2008)
27. W. Wang, S. Fujita, S.S. Wong, RESET mechanism of TiO_x resistance-change memory device. IEEE Electron Device Lett. **30**, 733–735 (2009)
28. K.M. Kim, C.S. Hwang, The conical shape filament growth model in unipolar resistance switching of TiO_2 thin film. Appl. Phys. Lett. **94**, 122109 (2009)
29. T.-N. Fang, S. Kaza, S. Haddad, A. Chen, Y.-C. Wu, Z. Lan, S. Avanzino, D. Liao, C. Gopalan, S. Choi, S. Mahdavi, M. Buynoski, Y. Lin, C. Marrian, C. Bill, M. VanBuskirk, M. Taguchi, Erase mechanism for copper oxide resistive switching memory cells with nickel electrode. IEDM Tech. Dig. 789–792 (2006)
30. H.Y. Lee, P.S. Chen, T.Y. Wu, Y.S. Chen, C.C. Wang, P.J. Tzeng, C.H. Lin, F. Chen, C.H. Lien, M.-J. Tsai, Low power and high speed bipolar switching with a thin reactive Ti buffer layer in robust HfO_2 based RRAM. IEDM Tech. Dig. 297–300 (2008)
31. Y.S. Chen, H.Y. Lee, P.S. Chen, P.Y. Gu, C.W. Chen, W.P. Lin, W.H. Liu, Y.Y. Hsu, S.S. Sheu, P.C. Chiang, W.S. Chen, F.T. Chen, C.H. Lien, M.-J. Tsai, Highly scalable hafnium oxide memory with improvements of resistive distribution and read disturb immunity. IEDM Tech. Dig. 105–108 (2009)
32. J.J. Yang, M.-X. Zhang, J.P. Strachan, F. Miao, M.D. Pickett, R.D. Kelley, G. Medeiros-Ribeiro, R.S. Williams, High switching endurance in TaO_x memristive devices. Appl. Phys. Lett. **97**, 232102 (2010)
33. M.-J. Lee, C.B. Lee, D. Lee, S.R. Lee, M. Chang, J.H. Hur, Y.-B. Kim, C.-J. Kim, D.H. Seo, S. Seo, U.-I. Chung, I.-K. Yoo, K. Kim, A fast, high-endurance and scalable non-volatile memory device made from asymmetric Ta_2O_{5-x}/TaO_{2-x} bilayer structures. Nat. Mater. **10**, 625–630 (2011)
34. K. Tsunoda, K. Kinoshita, H. Noshiro, Y. Yamazaki, T. Iizuka, Y. Ito, A. Takahashi, A. Okano, Y. Sato, T. Fukano, M. Aoki, Y. Sugiyama, IEDM Tech. Dig. 767–770 (2007)
35. Y. Sato, K. Tsunoda, K. Kinoshita, H. Noshiro, M. Aoki, Y. Sugiyama, Sub-100 μA reset current of nickel oxide resistive memory through control of filamentary conductance by current limit of MOSFET. IEEE Trans. Electron Devices **55**, 1185–1191 (2008)
36. K. Kinoshita, K. Tsunoda, Y. Sato, H. Noshiro, S. Yagaki, M. Aoki, Y. Sugiyama, Reduction in the reset current in a resistive random access memory consisting of NiO_x brought about by reducing a parasitic capacitance. Appl. Phys. Lett. **93**, 033506 (2008)
37. F. Nardi, D. Ielmini, C. Cagli, S. Spiga, M. Fanciulli, L. Goux, D.J. Wouters, Control of filament size and reduction of reset current below 10 μA in NiO resistance switching memories. Solid State Electron. **58**, 42–47 (2011)
38. Y. Wu, B. Lee, H.-S.P. Wong, Al_2O_3-based RRAM using atomic layer deposition (ALD) with 1 μA reset current. IEEE Electron Device Lett. **31**, 1449–1441 (2010)
39. C.H. Cheng, A. Chin, F.S. Yeh, High performance ultra-low energy RRAM with good retention and endurance. IEDM Tech. Dig. 448–491 (2010)
40. C.H. Ho, C.-L. Hsu, C.-C. Chen, J.-T. Liu, C.-S. Wu, C.-C. Huang, C. Hu, F.-L. Yang, 9 nm Half-pitch functional resistive memory cell with < 1 μA programming current using thermally oxidized sub-stoichiometric WO_x film. IEDM Tech. Dig. 436–439 (2010)
41. D. Ielmini, C. Cagli, F. Nardi, Resistance transition in metal oxides induced by electronic threshold switching. Appl. Phys. Lett. **94**, 063511 (2009)
42. H.Y. Lee, Y.S. Chen, P.S. Chen, P.Y. Gu, Y.Y. Hsu, S.M. Wang, W.H. Liu, C.H. Tsai, S.S. Sheu, P.C. Chiang, W.P. Lin, C.H. Lin, W.S. Chen, F.T. Chen, C.H. Lien, M.-J. Tsai, Evidence and solution of over-RESET problem for HfO_x based resistive memory with sub-ns switching speed and high endurance. IEDM Tech. Dig. 460–463 (2010)

43. F. Nardi, S. Balatti, S. Larentis, D. Ielmini, Complementary switching in metal oxides: Toward diode-less crossbar RRAMs. IEDM Tech. Dig. 709–712 (2011)

44. E. Linn, R. Rosezin, C. Kügeler, R. Waser, Complementary resistive switches for passive nanocrossbar memories. Nat. Mater. **9**, 403–406 (2010)

45. D. Ielmini, F. Nardi, C. Cagli, Universal reset characteristics of unipolar and bipolar metal-oxide RRAM. IEEE Trans. Electron Devices **58**, 3246–3253 (2011)

46. R. Rosezin, E. Linn, L. Nielen, C. Kügeler, R. Bruchhaus, R. Waser, Integrated complementary resistive switches for passive high-density nanocrossbar arrays. IEEE Electron Device Lett. **32**, 191–193 (2011)

47. J.H. Oh, J.H. Park, Y.S. Lim, H.S. Lim, Y.T. Oh, J.S. Kim, J.M. Shin, J.H. Park, Y.J. Song, K.C. Ryoo, D.W. Lim, S.S. Park, J.I. Kim, J.H. Kim, J. Yu, F. Yeung, C.W. Jeong, J.H. Kong, D.H. Kang, G.H. Koh, G.T. Jeong, H.S. Jeong, K. Kim, Full integration of highly manufacturable 512Mb PRAM based on 90 nm technology. IEDM Tech. Dig. 515–518 (2006)

48. Y. Sasago, M. Kinoshita, T. Morikawa, K. Kurotsuchi, S. Hanzawa, T. Mine, A. Shima, Y. Fujisaki, H. Kume, H. Moriya, N. Takaura, K. Torii, Cross-point phase change memory with $4F^2$ cell size driven by low-contact resistivity poly-Si diode. Symp. VLSI Tech. Dig. 24–25 (2009)

49. I.G. Baek, D.C. Kim, M.J. Lee, H.-J. Kim, E.K. Yim, M.S. Lee, J.E. Lee, S.E. Ahn, S. Seo, J.H. Lee, J.C. Park, Y.K. Cha, S.O. Park, H.S. Kim, I.K. Yoo, U.-I. Chung, J.T. Moon, B.I. Ryu, Multi-layer cross-point binary oxide resistive memory (OxRRAM) for post-NAND storage application. IEDM Tech. Dig. 750–753 (2005)

50. M.-J. Lee, Y. Park, B.-S. Kang, S.-E. Ahn, C. Lee, K. Kim, W. Xianyu, G. Stefanovich, J.-H. Lee, S.-J. Chung, Y.-H. Kim, C.-S. Lee, J.-B. Park, I.-K. Yoo, 2-stack 1D-1R cross-point structure with oxide diodes as switch elements for high density resistance RAM applications. IEDM Tech. Dig. 771–774 (2007)

51. M.-J. Lee, Y. Park, D.-S. Suh, E.-H. Lee, S. Seo, D.-C. Kim, R. Jung, B.-S. Kang, S.-E. Ahn, C.B. Lee, D.H. Seo, Y.-K. Cha, Two series oxide resistors applicable to high speed and high density nonvolatile memory. Adv. Mater. **19**, 3919–3923 (2007)

52. B.S. Kang, S.-E. Ahn, M.-J. Lee, G. Stefanovich, K.H. Kim, W.X. Xianyu, C.B. Lee, Y. Park, I.G. Baek, B.H. Park, High current-density $CuO_x/InZnO_x$ thin-film diodes for cross-point memory applications. Adv. Mater. **20**, 3066–3069 (2008)

53. G. Tallarida, N. Huby, B. Kutrzeba-Kotowska, S. Spiga, M. Arcari, G. Csaba, P. Lugli, A. Redaelli, R. Bez, Low temperature rectifying junctions for crossbar non-volatile memory devices, in IEEE International Memory Workshop Proceedings, pp. 6–8 (2009)

54. D. Kau, S. Tang, I.V. Karpov, R. Dodge, B. Klehn, J.A. Kalb, J. Strand, A. Diaz, N. Leung, J. Wu, S. Lee, T. Langtry, K.-W. Chang, C. Papagianni, J. Lee, J. Hirst, S. Erra, E. Flores, N. Righos, H. Castro, G. Spadini, A stackable cross point phase change memory. IEDM Tech. Dig. 617–620 (2009)

55. K. Gopalakrishnan, R.S. Shenoy, C.T. Rettner, K. Virwani, D.S. Bethune, R.M. Shelby, G.W. Burr, A. Kellock, R.S. King, K. Nguyen, A.N. Bowers, M. Jurich, B. Jackson, A.M. Friz, T. Topuria, P.M. Rice, B.N. Kurdi, Highly scalable novel access device based on mixed ionic electronic conduction (MIEC) materials for high density phase change memory (PCM) arrays. Symp. VLSI Tech. Dig. 205–206 (2010)

56. R.S. Shenoy, K. Gopalakrishnan, B. Jackson, K. Virwani, G.W. Burr, C.T. Rettner, A. Padilla, D.S. Bethune, R.M. Shelby, A.J. Kellock, M. Breitwisch, E.A. Joseph, R. Dasaka, R.S. King, K. Nguyen, A.N. Bowers, M. Jurich, A.M. Friz, T. Topuria, P.M. Rice, B.N. Kurdi, Endurance and scaling trends of novel access-devices for multi-layer crosspoint-memory based on mixed-ionic-electronic-conduction (MIEC) materials. Symp. VLSI Tech. Dig. 94–95 (2011)

57. M. Son, J. Lee, J. Park, J. Shin, G. Choi, S. Jung, W. Lee, S. Kim, S. Park, H. Hwang, Excellent selector characteristics of nanoscale VO_2 for high-density bipolar ReRAM applications. IEEE Electron Device Lett. **32**, 1579–1581 (2011)

58. D. Ielmini, S. Spiga, F. Nardi, C. Cagli, A. Lamperti, E. Cianci, M. Fanciulli, Scaling analysis of submicrometer nickel-oxide-based resistive switching memory devices. J. Appl. Phys. **109**, 034406 (2011)
59. R. Yasuhara, K. Fujiwara, K. Horiba, H. Kumigashira, M. Kotsugi, M. Oshima, H. Takagi, Inhomogeneous chemical states in resistance-switching devices with a planar-type Pt/CuO/Pt structure. Appl. Phys. Lett. **95**, 012110 (2009)
60. C.H. Kim, H.B. Moon, S.S. Min, Y.H. Jang, J.H. Cho, Nanoscale formation mechanism of conducting filaments in NiO thin films. Solid State Commun. **149**, 1611–1615 (2009)
61. D. Ielmini, Modeling the universal set/reset characteristics of bipolar RRAM by field- and temperature-driven filament growth. IEEE Trans. Electron Devices **58**, 4309–4317 (2011)
62. U. Russo, D. Ielmini, C. Cagli, A.L. Lacaita, Filament conduction and reset mechanism in NiO-based resistive-switching memory (RRAM) devices. IEEE Trans. Electron Devices **56**, 186–192 (2009)
63. C. Cagli, F. Nardi, D. Ielmini, Modeling of set/reset operations in NiO-based resistive-switching memory (RRAM) devices. IEEE Trans. Electron Devices **56**, 1712–1720 (2009)
64. Y.H. Tseng, C.-E. Huang, C.-H. Kuo, Y.-D. Chih, C.J. Lin, High density and ultra small cell size of contact ReRAM (CR-RAM) in 90nm CMOS logic technology and circuits. IEDM Tech. Dig. 109–112 (2009)
65. Y.H. Tseng, W.C. Shen, C.-E. Huang, C.J. Lin, Y.-C. King, Electron Trapping effect on the switching behavior of contact RRAM devices through random telegraph noise analysis. IEDM Tech. Dig. 636–639 (2010)
66. D.S. Jeong, H. Schroeder, R. Waser, Coexistence of bipolar and unipolar resistive switching behaviors in a Pt/TiO$_2$/Pt stack. Electrochem. Solid State Lett. **10**, G51–G53 (2007)
67. H. Schroeder, D.S. Jeong, Resistive switching in a Pt/TiO$_2$/Pt thin film stack—a candidate for a non-volatile ReRAM. Microelectron. Eng. **84**, 1982–1985 (2007)
68. L. Goux, J.G. Lisoni, M. Jurczak, D.J. Wouters, L. Courtade, C. Muller, Coexistance of the bipolar and unipolar resistive switching modes in NiO cells made by thermal oxidation of Ni layers. J. Appl. Phys. **107**, 024412 (2010)
69. L. Goux, Y. Chen, L. Pantisano, X. Wang, G. Groeseneken, M. Jurczak, D.J. Wouters, On the gradual unipolar and bipolar resistive switching of TiN\HfO$_2$\Pt memory systems. Electrochem. Solid State Lett. **13**, G54–G56 (2010)
70. D.C. Gilmer, G. Bersuker, H.-Y. Park, C. Park, B. Butcher, W. Wang, P.D. Kirsch, R. Jammy, Effects of RRAM stack configuration on forming voltage and current overshoot, in IEEE International Memory Workshop Proceedings, pp. 123–126 (2011)
71. J. Park, S. Jung, J. Lee, W. Lee, S. Kim, J. Shin, H. Hwang, Resistive switching characteristics of ultra-thin TiO$_x$. Microelectron. Eng. **88**, 1136–1139 (2011)
72. J. Lee, J. Shin, D. Lee, W. Lee, S. Jung, M. Jo, J. Park, K.P. Biju, S. Kim, S. Park, H. Hwang, Diode-less nano-scale ZrO$_x$/HfO$_x$ RRAM device with excellent switching uniformity and reliability for high-density cross-point memory applications. IEDM Tech. Dig. 442–445 (2010)
73. L. Goux, J.G. Lisoni, X.P. Wang, M. Jurczak, D.J. Wouters, Optimized Ni oxidation in 80-nm contact holes for integration of forming-free and low-power Ni/NiO/Ni memory cells. IEEE Trans. Electron Devices **56**, 2363–2368 (2009)
74. D. Ielmini, Filamentary-switching model in RRAM for time, energy and scaling projections. IEDM Tech. Dig. 409–412 (2011)
75. U. Russo, D. Kalamanathan, D. Ielmini, A.L. Lacaita, M. Kozicki, Study of multilevel programming in programmable metallization cell (PMC) memory. IEEE Trans. Electron Devices **56**, 1040–1047 (2009)
76. U. Russo, D. Ielmini, C. Cagli, A.L. Lacaita, Self-accelerated thermal dissolution model for reset programming in NiO-based resistive switching memory (RRAM) devices. IEEE Trans. Electron Devices **56**, 193–200 (2009)
77. D. Ielmini, C. Cagli, F. Nardi, Physical models of size-dependent nanofilament formation and rupture in NiO resistive switching memories. Nanotechnology **22**, 254022 (2011)

78. V.V. Zhirnov, R.K. Cavin III, S. Menzel, E. Linn, S. Schmelzer, D. Brauhaus, C. Schindler, R. Waser, Memory devices: Energy-space-time tradeoffs. Proc. IEEE **98**, 2185–2200 (2010)
79. S. Yu, H.-S.P. Wong, Compact modeling of conducting-bridge random-access memory (CBRAM). IEEE Trans. Electron Devices **58**, 1352–1360 (2011)
80. J. Park, M. Jo, E.M. Bourim, J. Yoon, D.J. Seong, J. Lee, W. Lee, H. Hwang, Investigation of state stability of low-resistance state in resistive memory. IEEE Electron Device Lett. **31**, 485–487 (2010)
81. D. Ielmini, F. Nardi, C. Cagli, A.L. Lacaita, Size-dependent retention time in NiO-based resistive switching memories. IEEE Electron Device Lett. **31**, 353–355 (2010)
82. D. Ielmini, Universal set/reset characteristics of metal-oxide resistance switching memories. ECS Trans. **35**, 581–596 (2011)
83. D. Ielmini, F. Nardi, C. Cagli, Resistance-dependent amplitude of random telegraph signal noise in resistive switching memories. Appl. Phys. Lett. **96**, 053503 (2010)